Supplement of Atmos. Chem. Phys., 24, 8441–8455, 2024
https://doi.org/10.5194/acp-24-8441-2024-supplement

Atmospheric Chemistry and Physics
Open Access

Supplement of

Large contributions of soil emissions to the atmospheric nitrogen budget and their impacts on air quality and temperature rise in North China

Tong Sha et al.

Correspondence to: Tong Sha (tong-sha@sust.edu.cn) and Jun Wang (jun-wang-1@uiowa.edu)

S1. Approach of converting the MEIC inventory to the model-ready formats.

The MEIC inventory used in this study has a spatial resolution of 0.25 ° × 0.25 ° and is constructed on an equal latitude-longitude grid. The model domain, however, employs a Lambert projection, which results in a misalignment between these two grid systems. We thus implement a spatial interpolation method to reallocate emission fluxes to the model grid. The descriptions are as follows:

Under the Lambert projection, the model grids are rectangular, while the MEIC grids are deformed, approximating a trapezoid shape. For calculating the emission of each model grid, we determine which MEIC grid may fall in that grid, based on their central latitude and longitude coordinates, and then apply the principle that the ratio of emissions is equivalent to the ratio of areas between the model grid and MEIC grid. The area of the MEIC grid is denoted as A and its corresponding emission is denoted as E, and the area of the model grid is denoted as a, thus the emission fluxes of model grid e are expressed as $e = E \times a / A$. However, if the spatial resolution of the simulation domain is coarser than MEIC, the model grid often falls within multiple MEIC grids and this method would have errors. We thus divide the coarser model grid into $n \times n$ finer subgrids. Since the spatial resolution of the nested domain is 9 km in this study, we choose n as 9. We apply the aforementioned method to calculate the emissions of each finer model subgrid, and then sum up the emissions of $n \times n$ finer subgrids to obtain the total emissions of the model grid. This method ensures a more accurate allocation of MEIC emission to the model grid, despite different spatial resolutions of the simulation domain.

S2. Parameterization of HONO sources

In the present study, we incorporated five additional HONO sources in the WRF-Chem model, as described below.

1. Direct traffic emissions

The traffic emission was calculated by a HONO/NO_x ratio of 1.7% (Rappenglück et al., 2013), which is the same as the setting of (Zhang et al., 2019).

2. The HONO source from soil emissions

See section 2.1.2 in the manuscript.

3. Heterogeneous source on aerosol surface

$$2\mathrm{NO_2} + \mathrm{H_2O} \xrightarrow{aerosol\ \ surface} \mathrm{HONO} + \mathrm{HNO_3} \quad (k_a) \tag{R1}$$

Most studies suggested that the heterogeneous reaction of NO_2 to HONO was first order in NO_2 (Finlayson-Pitts et al., 2003; Saliba et al., 2000), thus for the NO_2 heterogeneous reaction on the aerosol surface, the first-order reaction rate constant k_a is estimated by (Li et al., 2010) and (Zhang et al., 2016) as follows:

$$k_a = \frac{1}{4} \cdot v_{\mathrm{NO2}} \cdot (\frac{S_a}{V}) \cdot \gamma_{\mathrm{a-NO2}} \tag{S1}$$

where v_{NO2} is the mean molecular velocity of NO_2 (m s^{-1}), S_a/V is the aerosol surface to volume ratio (m^{-1}) representing the surface available for heterogeneous reaction. $\gamma_{\mathrm{a-NO2}}$ is the uptake coefficient of NO_2 at the aerosol surface, which was set to be 1×10^{-6} for nighttime, and a higher value of 2×10^{-5} applied for daytime when the light intensity (LI) was lower than 400 W m^{-2}, whereas we linearly scaled it with solar radiation when the light intensity was higher than 400 W m^{-2} (equation 2).

$$\gamma_{\mathrm{a-NO2}} = \begin{cases} 1 \times 10^{-6} \ \ (\text{nighttime}) \\ 2 \times 10^{-5} \cdot \left(\frac{\mathrm{LI}}{400}\right) \ \ (\text{daytime}, \mathrm{LI} \geq 400\mathrm{W\ \ m^{-2}}) \\ 2 \times 10^{-5} \ \ (\text{daytime}, \mathrm{LI} < 400\mathrm{W\ \ m^{-2}}) \end{cases} \tag{S2}$$

4. Heterogeneous source on ground surface

$$2\mathrm{NO_2} + \mathrm{H_2O} \xrightarrow{ground\ \ surface} \mathrm{HONO} + \mathrm{HNO_3} \quad (k_g) \tag{R2}$$

For the NO_2 heterogeneous reaction on ground surface (R2), the first-order reaction rate constant k_g is estimated by (Zhang et al., 2016) as follows:

$$k_g = \frac{1}{8} \cdot v_{\mathrm{NO2}} \cdot (\frac{S_g}{V}) \cdot \gamma_{\mathrm{g-NO2}} \tag{3}$$

where v_{NO2} is the mean molecular velocity of NO_2 (m s^{-1}), S_g/V represents the ground surface to volume ratio. Over the urban areas as defined by the MODIS land use data, we adopted a constant S_g/V value of 0.3 m^{-1}. For the vegetation-covered areas, the leaf area index (LAI, m^2/m^2) and the height of the first model layer (H, m) were used to estimate the surface area to volume ratio following the method in (Sarwar et al., 2008):

$$\frac{S_g}{V} = \frac{2\times\mathrm{LAI}}{H} \tag{4}$$

$\gamma_{\mathrm{g-NO2}}$ is the uptake coefficient of NO_2 at the ground surface and is assumed to be the same as that for aerosol surface. The heterogeneous reaction of NO_2 on the ground surface was only considered within the first model layer, whereas that on the aerosol surface was treated in all model layers.

5. Inorganic nitrate photolysis

The photolysis reaction of particulate nitrate in the atmosphere to produce HONO and NO_2 (R3) was added in the WRF-Chem model following the work of (Fu et al., 2019).

$$p\mathrm{NO_3} + hv \rightarrow 0.67\mathrm{HONO} + 0.33\mathrm{NO_2} \tag{R3}$$

The photolysis rate of particulate nitrate was estimated by a $J_{\mathrm{nitrate}}/J_{\mathrm{HNO3}}$ ratio of $\frac{8.3\times10^{-5}}{7\times10^{-7}}$, where J_{HNO3} is the photolysis rate of gaseous HNO_3 simulated online in the model.

Table S1 Total annual N fertilizer application from 2006 to 2018 (unit: 10 Gg N yr^{-1}), and the adjustment coefficient (2006 vs. 2018, unit: %) for N fertilizer application in each province.

Province	**2006**	**2007**	**2008**	**2009**	**2010**	**2011**	**2012**	**2013**	**2014**	**2015**	**2016**	**2017**	**2018**	**2006vs.2018**
Neimenggu	64	68	73	80	80	81	83	89	97	99	98	95	86	34.5
Gansu	37	38	38	38	38	38	40	40	41	41	39	34	33	-9.6
Ningxia	16	17	17	17	18	18	18	19	18	17	17	17	16	4.5
Shaanxi	76	81	81	87	88	91	98	99	96	94	92	90	89	16.2
Shanxi	41	41	40	39	40	39	39	38	36	34	32	28	25	-38
Hebei	155	156	153	153	153	152	152	151	151	148	145	140	114	-26.2
Beijing	8	7	7	7	7	7	6	6	5	5	4	4	3	-61.3
Tianjin	12	13	12	12	12	11	11	11	11	10	9	7	6	-53.6
Henan	235	239	240	239	244	245	246	244	241	239	228	220	202	-14.3
Shandong	194	193	170	165	163	159	160	158	154	151	146	139	131	-32.5
Jiangsu	183	183	181	182	180	174	169	166	164	162	158	151	146	-20.4
Anhui	112	111	112	112	112	114	114	114	112	108	105	101	96	-14.4
Huibei	140	143	149	154	156	159	159	153	146	139	134	128	113	-19.5
Chongqing	46	48	50	50	49	50	50	50	50	50	48	47	46	-1.1
Sichuan	125	128	129	131	130	129	128	126	126	125	122	117	112	-10.1
Liaoning	63	65	66	67	68	70	68	70	68	66	60	57	55	-13.5

Table S2. Soil categories used in (Oswald et al., 2013).

No.	Soil Category in Oswald et al. (2013)
S1	eucalyptus forest, Grose Valley, Australia
S2	tropical rain forest, Suriname
S3	coniferous forest, Hohenpeißenberg, Germany
S4	coniferous forest, Fichtelgebirge, Germany
S5	pasture, Hawkesbury River flood plain, Australia
S6	open woody savannah, Dahra, Senegal
S7	open woody savannah, Agoufou, Mali
S8	grassland, Mainz-Finthen, Germany
S9	pasture, Hohenpeißenberg, Germany
S10	stone desert, Ruta B 376, Chile
S11	maize field, Grignon, France
S12	wheat field, Mainz-Finthen, Germany
S13	jujube field, Qiemo, China
S14	cotton field, Qiemo, China
S15	jujube field, Mingfeng, China
S16	stone desert, Sache, China
S17	cotton field, Milan, China

Table S3. Emission factor of 20 soil biomes based on MODIS land cover types.

ID	MODIS land cover type	MEDIUM	HIGH	LOW
1	Evergreen needleleaf forest	S3, S4	S3	S4
2	Evergreen broadleaf forest	S2	S2	S2
3	Deciduous needleleaf forest	S3, S4	S3	S4
4	Deciduous broadleaf forest	S1	S1	S1
5	Mixed forest	S1, S2, S3, S4	S2	S4
6	Closed shrublands	S6, S7, S8	S6	S8
7	Open shrublands	S6, S7	S6	S7
8	Woody savannas	--	--	--
9	Savannas	S6, S7	S6	S7
10	Grasslands	S8	S8	S8
11	Permanent wetlands	--	--	--
12	Croplands	S5, S9, S11, S12, S14, S17	S12	S9
13	Urban and built-up	--	--	--
14	Cropland/Natural vegetation mosaic	S8, S5, S9, S11, S12, S14, S17	S12	S9
15	Snow and ice	--	--	--
16	Barren or sparsely vegetated	S16, S10	S10	S16
17	water	--	--	--
18	Wooded tundra	--	--	--
19	Mixed tundra	--	--	--
20	Barren Tundra	--	--	--

Table S4. The optimum SHONO fluxes used in this study and other literature.

ID	MODIS land cover type	Optimum SHONO fluxes ($ng\ m^{-2}\ s^{-1}$)	References (land cover type in local scale)
1	Evergreen needleleaf forest	**0.549**	this study
2	Evergreen broadleaf forest	**2.872**	this study
3	Deciduous needleleaf forest	**0.549**	this study
4	Deciduous broadleaf forest	**0.887**	this study
5	Mixed forest	**1.214**	this study
		1.3	Zhou et al. (2011)
		0.01-104.72 (mean=16.45)	Wu et al. (2022)
		0.2-208 (mean=50)	Wang et al. (2023)
6	Closed shrublands	**20.57**	this study
7	Open shrublands	**29.779**	this study
8	Woody savannas	--	--
9	Savannas	**9.926**	this study
		1.1	Weber B (2015)
10	Grasslands	**2.154**	this study
		1.0	Twigg et al. (2011)
		0.1-74.27(mean =17.57)	Wu et al. (2022)
11	Permanent wetlands	--	--
12	Croplands	**30.036**	this study
		1.42-376.01(mean =119.8)	Wu et al. (2019, 2022)
		0.84±2.38	Meng et al. (2022)
		-1.32-7.69 (mean=2.94)	Tang et al. (2020)
		3.21	Xue et al. (2019)
		16-484	Wang et al. (2023)
13	Urban and built-up	--	--
14	Cropland/Natural vegetation mosaic	**25.847**	this study
15	Snow and ice	--	--
16	Barren or sparsely vegetated	**14.742**	this study

		1.5	Weber B (2015)
		5.38-288.23 (mean=57.06)	Wu et al. (2022)
17	water	--	--
18	Wooded tundra	--	--
19	Mixed tundra	--	--
20	Barren Tundra	--	--

Table S5. Contribution of soil NO_x and HONO emissions to monthly average surface concentrations of NO_2 and HONO (unit: %) in July 2018.

Contribution	Surface NO_2 concentrations			Surface HONO concentrations		
	Study region (CL)	BTH(CL)	FWP(CL)	Study region (CL)	BTH(CL)	FWP(CL)
SNO_x	30.3(33.2)	37.1(39.5)	31.8(38.6)	6.2(5.7)	7.8(7.6)	4.95(4.2)
SHONO	3.1(2.3)	1.8(1.75)	2.7(3.1)	35.6 (38.7)	36.7(38.6)	38.0(42.7)
Soil Nr	32.7(34.7)	38.4(40.5)	33.9(41.3)	38.2(20.0)	40.3(42.0)	40.1(44.6)

Table S6. Effect of soil NO_x and HONO emissions on monthly average surface concentrations of MDA8 O_3, max-1h OH, and nitrate in BTH and FWP region during July 2018 (unit: %).

Change	MDA8 O_3			max-1h ·OH			nitrate		
	Study region (CL)	BTH (CL)	FWP (CL)	Study region (CL)	BTH (CL)	FWP (CL)	Study region (CL)	BTH (CL)	FWP (CL)
Soil NOx	15.3 (17.4)	13.9 (15.0)	14.6 (15.6)	-31.3 (-21.6)	-28.4 (-13.5)	-38.6 (-24.8)	17.8 (22.4)	29.6 (41.3)	27.6 (32.8)
Soil HONO	3.3 (3.0)	3.5 (3.8)	2.8 (3.1)	10.0 (13.4)	9.3 (13.1)	10.3 (17.5)	10.4 (11.3)	10.9 (14.2)	13.5 (15.2)
Soil Nr	18.2 (20.0)	16.9 (18.1)	17.2 (18.6)	-24.3 (-12.5)	-22.6 (-4.4)	-32.2 (-13.6)	31.8 (35.8)	42.4 (57.8)	42.7 (49.9)

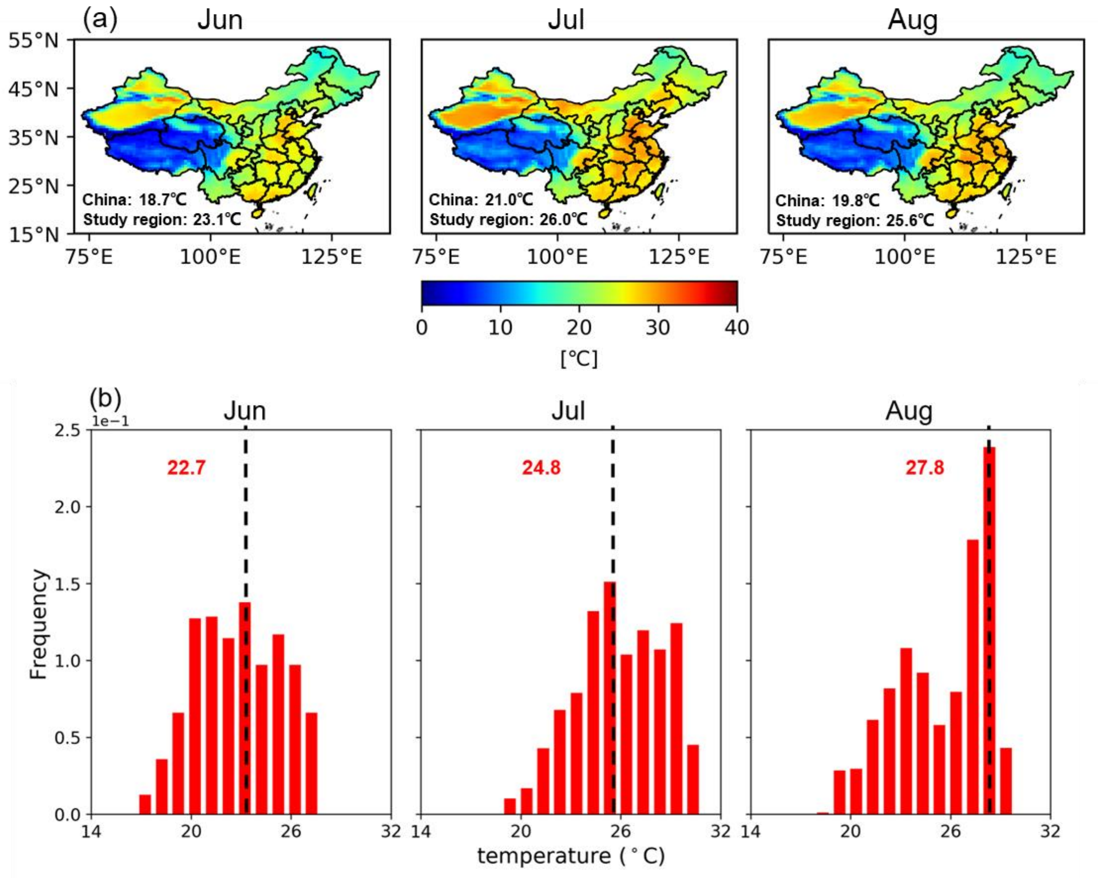

Figure S1. (a) Distribution of monthly average air temperature at 2m (T2) from the MERRA-2 dataset during June-August 2018. The statistics over lower left corner are the monthly average T2 over China and the study region. (b) Frequency of the monthly average T2 in the study region during June-August 2018. The statistics on each panel are the T2 corresponding to the highest frequency.

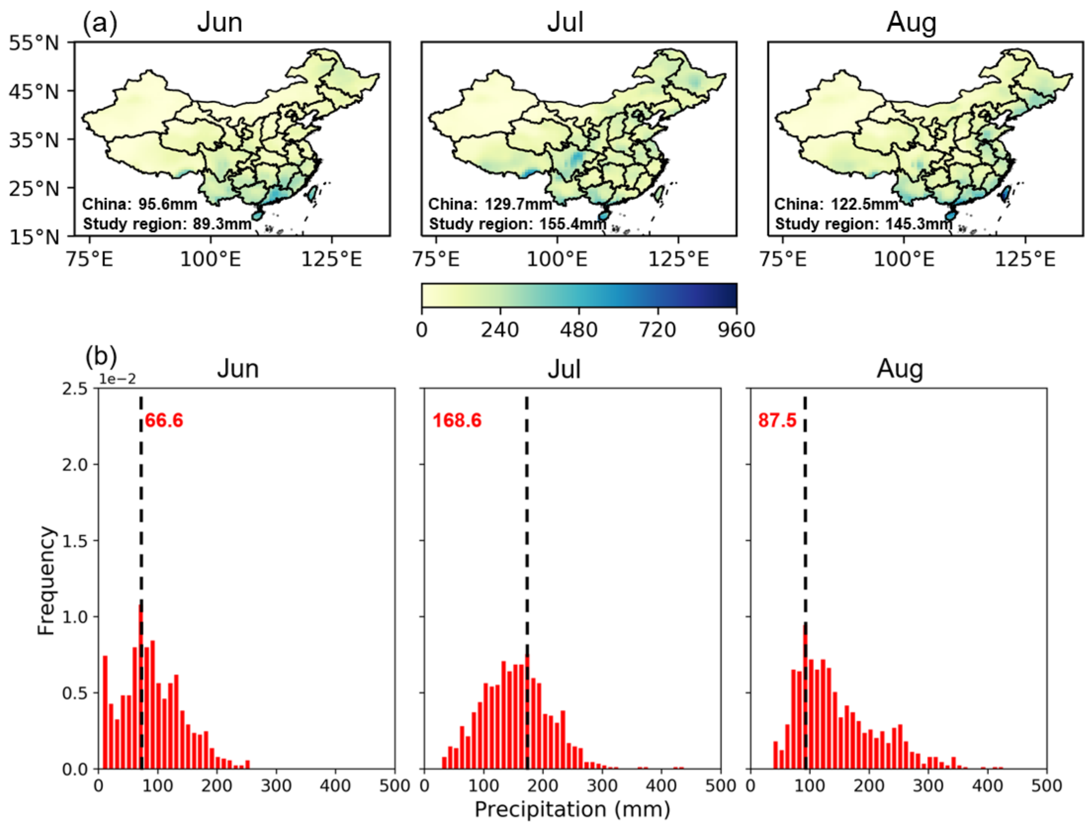

Figure S2. Distribution of monthly total precipitation from the MERRA-2 dataset during June-August 2018. The statistics over lower left corner are the total monthly precipitation over China and the study region. (b) Frequency of the monthly total precipitation in the study region during June-August 2018. The statistics on each panel are the total precipitation amount corresponding to the highest frequency.

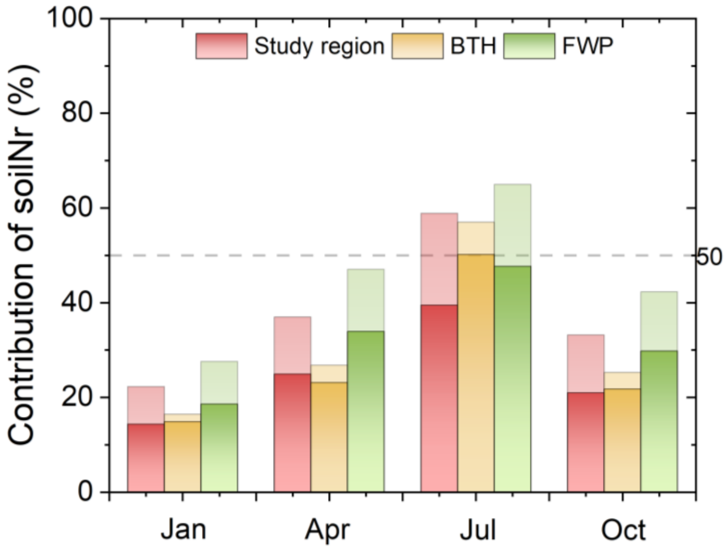

Figure S3. Monthly proportion of soil Nr emissions to anthropogenic NO_x emissions during January, April, July, and October in the study region, BTH, and FWP regions. The darker columns with borders are statistics for the whole region, while the lighter columns are statistics for croplands. The gray horizontal dotted line in the figure represents a 50% proportion.

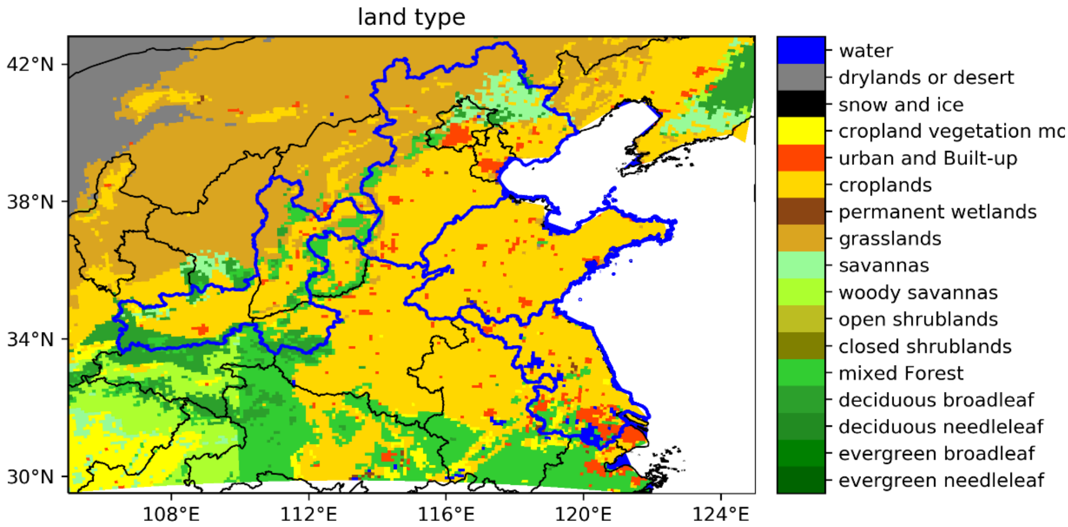

Figure S4. The land cover type over the simulation domain.

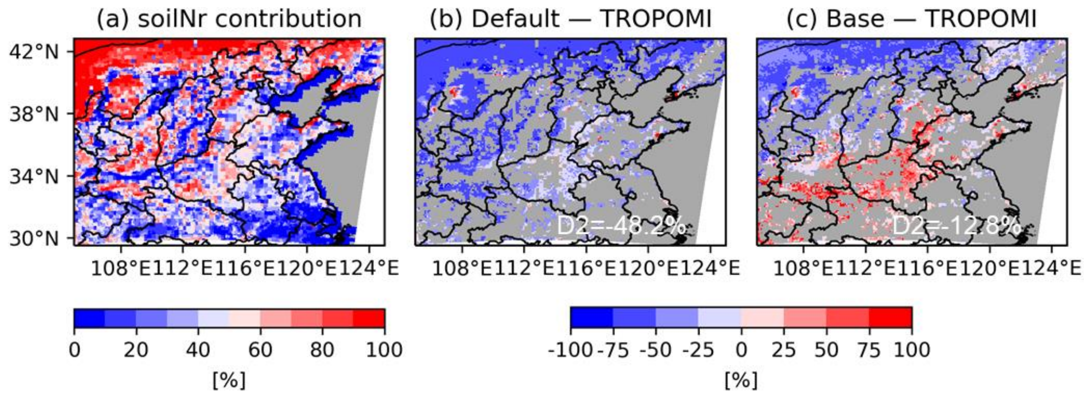

Figure S5. (a) Distribution of simulated contribution of soil Nr emissions to total Nr emissions, which includes the sources from anthropogenic emissions, soil emissions, and biomass burning. The difference of monthly mean tropospheric NO_2 VCD from TROPOMI observations and simulations ((b) Default, (c) Base). The grids where soil Nr emissions contributions are lower than 50% are masked to better compare the difference of observations and simulations in rural areas surrounding cities. Statistics in each panel are the mean value averaged over the study region in July 2018.

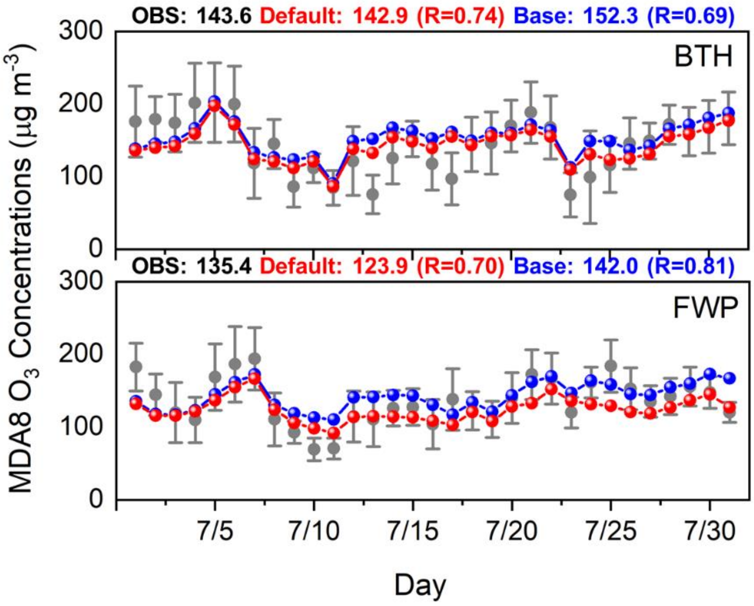

Figure S6. Time series of observed (grey circles with bars representing the standard deviations) and simulated (Default in red and Base in blue) surface MDA8 O_3 concentrations in the BTH and FWP regions in July 2018, with the mean value and temporal correlation coefficients (R) shown in the upper corner.

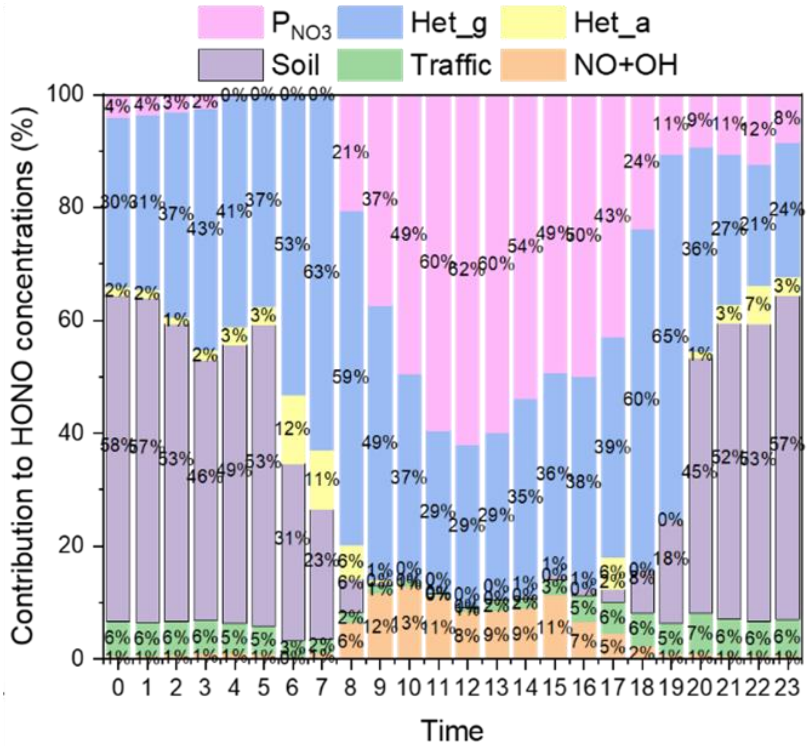

Figure S7. Average diurnal variations of contributions of different HONO sources to the simulated surface HONO at a rural station in Nanjing during July 2018. (P_{NO3}, Het_g, Het_a, Soil, Traffic, and NO+OH represent HONO sources from the inorganic nitrate photolysis in the atmosphere, NO_2 heterogeneous reactions on ground and aerosol surfaces, soil emissions, traffic emissions, and the gas-phase formation, respectively).

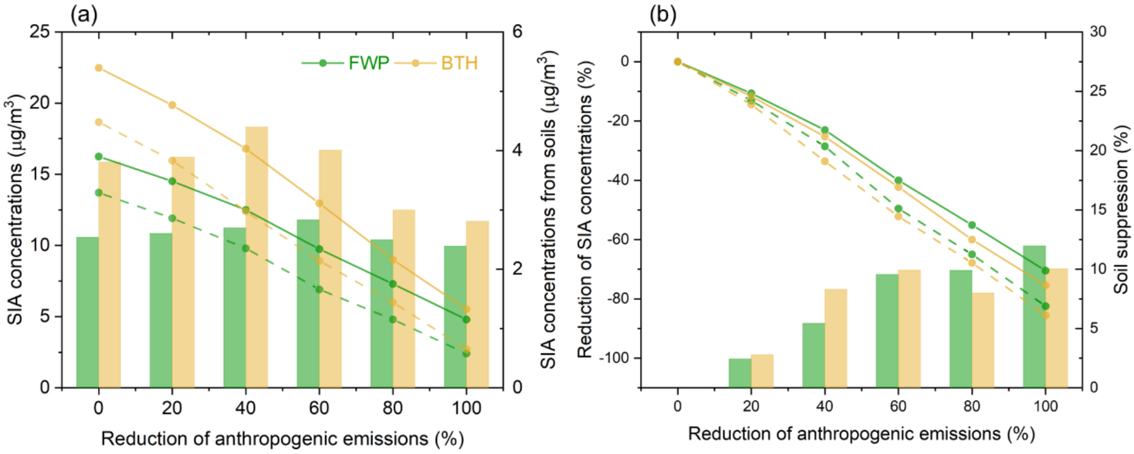

Figure S8. The responses of secondary inorganic aerosols (SIA) concentrations to the reductions of anthropogenic emissions (taking into account the SO_2, NO_x, primary $PM_{2.5}$, VOCs, and CO reduced by 20%, 40%, 60%, 80%, and 100%) relative to July 2018 levels in the presence (solid line) and absence (dotted line) of soil Nr emissions. (The lines in panels (a-b) are SIA concentrations and the relative reductions in SIA concentrations under different anthropogenic emission reductions, respectively. The bars (right y-axis) in panel (a) show the corresponding SIA concentrations from soil Nr emissions (denoted as SIA concentrations from soils) under different anthropogenic emission reductions, which are determined as the difference between the solid and dotted lines. The bars (right y-axis) in panel (b) show the suppression of SIA reduction due to the existence of soil Nr emissions (denoted as soil suppression), which are determined as the difference between the solid and dotted lines. Green lines and bars are the results in the FWP region, and the yellow are the results in the BTH region.)

Reference

Finlayson-Pitts, B. J., Wingen, L. M., Sumner, A. L., Syomin, D., and Ramazan, K. A.: The heterogeneous hydrolysis of NO_2 in laboratory systems and in outdoor and indoor atmospheres: An integrated mechanism, Phys. Chem. Chem. Phys., 5, 223-242, 10.1039/b208564j, 2003.

Fu, X., Wang, T., Zhang, L., Li, Q., Wang, Z., Xia, M., Yun, H., Wang, W., Yu, C., Yue, D., Zhou, Y., Zheng, J., and Han, R.: The significant contribution of HONO to secondary pollutants during a severe winter pollution event in southern China, Atmos. Chem. Phys., 19, 1-14, 10.5194/acp-19-1-2019, 2019.

Li, G., Lei, W., Zavala, M., Volkamer, R., Dusanter, S., Stevens, P., and Molina, L. T.: Impacts of HONO sources on the photochemistry in Mexico City during the MCMA-2006/MILAGO Campaign, Atmos. Chem. Phys., 10, 6551-6567, 10.5194/acp-10-6551-2010, 2010.

Meng, F., Qin, M., Fang, W., Duan, J., Tang, K., Zhang, H., Shao, D., Liao, Z., Feng, Y., Huang, Y., Ni, T., Xie, P., Liu, J., and Liu, W.: Measurement of HONO flux using the aerodynamic gradient method over an agricultural field in the Huaihe River Basin, China, J. Environ. Sci., 114, 297-307, 10.1016/j.jes.2021.09.005, 2022.

Oswald, R., Behrendt, T., Ermel, M., Wu, D., Su, H., Cheng, Y., Breuninger, C., Moravek, A., Mougin, E., Delon, C., Loubet, B., Pommerening-Röser, A., Sörgel, M., Pöschl, U., Hoffmann, T., Andreae, M. O., Meixner, F. X., and Trebs, I.: HONO Emissions from Soil Bacteria as a Major Source of Atmospheric Reactive Nitrogen, Science, 341, 1233-1235, 10.1126/science.1242266, 2013.

Rappenglück, B., Lubertino, G., Alvarez, S., Golovko, J., Czader, B., and Ackermann, L.: Radical precursors and related species from traffic as observed and modeled at an urban highway junction, J. Air Waste Manage. Assoc., 63, 1270-1286, 2013.

Saliba, N. A., Mochida, M., and Finlayson-Pitts, B. J.: Laboratory studies of sources of HONO in polluted urban atmospheres, Geophys. Res. Lett., 27, 3229-3232, 10.1029/2000gl011724, 2000.

Sarwar, G., Roselle, S. J., Mathur, R., Appel, W., Dennis, R. L., and Vogel, B.: A comparison of CMAQ HONO predictions with observations from the Northeast Oxidant and Particle Study, Atmos. Environ., 42, 5760-5770, 10.1016/j.atmosenv.2007.12.065, 2008.

Tang, K., Qin, M., Fang, W., Duan, J., Meng, F., Ye, K., Zhang, H., Xie, P., Liu, J., Liu, W., Feng, Y., Huang, Y., and Ni, T.: An automated dynamic chamber system for exchange flux measurement of reactive nitrogen oxides (HONO and NO_x) in farmland ecosystems of the Huaihe River Basin, China, Sci. Total Environ., 745, 140867, 10.1016/j.scitotenv.2020.140867, 2020.

Twigg, M. M., House, E., Thomas, R., Whitehead, J., Phillips, G. J., Famulari, D., Fowler, D., Gallagher, M. W., Cape, J. N., Sutton, M. A., and Nemitz, E.: Surface/atmosphere exchange and chemical interactions of reactive nitrogen compounds above a manured grassland, Agric. For. Meteorol., 151, 1488-1503, 10.1016/j.agrformet.2011.06.005, 2011.

Wang, Y., Fu, X., Wang, T., Ma, J., Gao, H., Wang, X., and Pu, W.: Large Contribution of Nitrous Acid to Soil-Emitted Reactive Oxidized Nitrogen and Its Effect on Air Quality, Environ. Sci. Technol., 57, 3516-3526, 10.1021/acs.est.2c07793, 2023.

Weber B, W. D., Tamm A, et al. : Biological soil crusts accelerate the nitrogen cycle through large NO and HONO emissions in drylands, Proc. Natl. Acad. Sci. U.S.A., 112(50): 15384-15389., 2015.

Wu, D., Horn, M. A., Behrendt, T., Müller, S., Li, J., Cole, J. A., Xie, B., Ju, X., Li, G., Ermel, M., Oswald, R., Fröhlich-Nowoisky, J., Hoor, P., Hu, C., Liu, M., Andreae, M. O., Pöschl, U., Cheng, Y., Su, H., Trebs, I., Weber, B., and Sörgel, M.: Soil HONO emissions at high moisture content are driven by microbial nitrate reduction to nitrite: tackling the HONO puzzle, ISME J., 13, 1688-1699, 10.1038/s41396-019-0379-y, 2019.

Wu, D., Zhang, J., Wang, M., An, J., Wang, R., Haider, H., Xu-Ri, Huang, Y., Zhang, Q., Zhou, F., Tian, H., Zhang, X., Deng, L., Pan, Y., Chen, X., Yu, Y., Hu, C., Wang, R., Song, Y., Gao, Z., Wang, Y., Hou, L., and Liu, M.: Global and Regional Patterns of Soil Nitrous Acid Emissions and Their Acceleration of Rural Photochemical Reactions, J. Geophys. Res.: Atmos., 127, 10.1029/2021jd036379, 2022.

Xue, C., Ye, C., Zhang, Y., Ma, Z., Liu, P., Zhang, C., Zhao, X., Liu, J., and Mu, Y.: Development and application of a twin open-top chambers method to measure soil HONO emission in the North China Plain, Sci. Total Environ., 659, 621-631, 10.1016/j.scitotenv.2018.12.245, 2019.

Zhang, J., An, J., Qu, Y., Liu, X., and Chen, Y.: Impacts of potential HONO sources on the concentrations of oxidants and secondary organic aerosols in the Beijing-Tianjin-Hebei region of China, Sci. Total Environ., 647, 836-852, 10.1016/j.scitotenv.2018.08.030, 2019.

Zhang, L., Wang, T., Zhang, Q., Zheng, J., Xu, Z., and Lv, M.: Potential sources of nitrous acid (HONO) and their impacts on ozone: A WRF-Chem study in a polluted subtropical region, J. Geophys. Res.: Atmos., 121, 3645-3662, 10.1002/2015jd024468, 2016.

Zhou, X., Zhang, N., TerAvest, M., Tang, D., Hou, J., Bertman, S., Alaghmand, M., Shepson, P. B., Carroll, M. A., Griffith, S., Dusanter, S., and Stevens, P. S.: Nitric acid photolysis on forest canopy surface as a source for tropospheric nitrous acid, Nat. Geosci., 4, 440-443, 10.1038/ngeo1164, 2011.